Interactions of $C^+(^2P_J)$ with rare gas atoms: Incipient chemical interactions, potentials and transport coefficients

William D. Tuttle,[a] Rebecca L. Thorington,[a] Larry A. Viehland,[b *] W. H. Breckenridge,[c]

and Timothy G. Wright [a **]

Abstract

Accurate interatomic potentials were calculated for the interaction of a singly-charged carbon cation, C^+, with a single rare gas atom, RG (RG = Ne–Xe). The RCCSD(T) method and basis sets of quadruple-ζ and quintuple-ζ quality were employed; each interaction energy is counterpoise corrected and extrapolated to the basis set limit. The lowest $C^+(^2P)$ electronic term of the carbon cation was considered, and the interatomic potentials calculated for the diatomic terms that arise from these: $^2\Pi$ and $^2\Sigma^+$. Additionally, the interatomic potentials for the respective spin-orbit levels were calculated, and the effect on the spectroscopic parameters was examined. In doing this, anomalously large spin-orbit splittings for RG = Ar–Xe were found, and this was investigated using multireference configuration interaction (MRCI) calculations. The latter indicated a small amount of RG → C^+ electron transfer and this was able to rationalize the observations. This is taken as evidence of an incipient chemical interaction, which was also examined via contour plots, Birge-Sponer plots and various population analyses across the C^+-RG series (RG = He–Xe), with the latter showing unexpected results. Trends in several spectroscopic parameters were examined as a function of the increasing atomic number of the RG atom. Finally, each set of RCCSD(T) potentials was employed including spin-orbit coupling to calculate transport coefficients for C^+ in RG, and the results compared to the limited available data.

Key words: carbon cation, rare gas, spectroscopy, bonding, ion transport

[a] School of Chemistry, University Park, University of Nottingham, Nottingham NG7 2RD, United Kingdom.

[b] Science Department, Chatham University, Pittsburgh, Pennsylvania 15232, USA

[c] Department of Chemistry, University of Utah, 315 South 1400 East, Room 2020, Salt Lake City, Utah 84112, USA.

* **Email**: Viehland@Chatham.edu

** **Email**: Tim.Wright@nottingham.ac.uk

1. Introduction

Carbon ions, C^+, appear in wide-ranging situations. They are thought to play a key role in the chemistry of the interstellar medium [1,2], and indeed the C^+-He complex has been proposed as being involved in a cooling mechanism for C^+ ions [3]. C^+ ions are present in the ionosphere of the Earth [4] and in the ionospheric regions of other planets [5]; they are also present in flames and plasmas [6] including in chemical vapour deposition (CVD) [7], and even have a use in radiotherapy [8].

In order for chemistry to be initiated, the reacting species must come together; hence, "pre-reactive" atomic or molecular complexes are often discussed as ways of interrogating these nascent interactions that occur prior to full chemical reaction. Although rather esoteric, the interactions of atomic cations with rare gas atoms are of interest as they are generally agreed to be amongst the simplest interactions that can be investigated, evolving from expected physical interactions when the rare gas is the very non-polarizable helium atom, to the possibility of chemical interactions for the more-polarizable Xe atom.

The first stage in investigating C^+-RG interactions is via the determination of the interatomic potentials. Once obtained, these can be used to determine various spectroscopic parameters and values of these and their trends can be used to make conclusions regarding the changing nature of the interaction, for example as the atomic number of the RG atom increases. Additionally, the electronic wavefunctions can be analysed to obtain populations and contours of electron density, which indicate whether electrons remain localized or are shared between the interacting species; such delocalization of electron density from one nuclear centre to another can be taken as indicating chemical interaction – although other significant, but more localized changes, such as hybridization, can also be considered as chemical effects. Interaction potentials are also important in the calculation of a range of quantities including collision cross sections – important in the calculation of ion transport data and atomic collisional energy transfer. In turn, these underpin loss mechanisms to walls in flow-tube experiments, transport of ions in plasmas, and cooling of interstellar clouds.

In the present paper, we extend our earlier work on the C^+-He complex [9] to the corresponding complexes with the heaver RG atoms, RG = Ne–Xe. In each case, we shall investigate the interatomic potentials that arise from the lowest atomic asymptotes of the open-shell C^+-RG complex, $C^+(^2P_J)$ + RG($^1S_0$). These arise from the closed-shell ground state configuration of the RG atom, and the lowest energy electronic configuration for the carbon cation: $1s^2 2s^2 2p^1$, when the spin-orbit interaction is included. From these interatomic potentials, we shall obtain accurate spectroscopic constants and transport coefficients, and investigate whether the spin-orbit (SO) interaction affects these significantly.

When a closed-shell RG atom interacts with C^+, degenerate atomic states may become split. In the present case, and initially in the absence of the spin-orbit interaction, the ^2P ground electronic term of C^+ gives rise to a lower $^2\Pi$ and a higher $^2\Sigma^+$ diatomic term. In the limited previous theoretical work,

these are the terms that have been investigated, but it is the spin-orbit levels that are present experimentally. Upon the inclusion of the spin-orbit (SO) interaction, the $C^+(^2P)$ term splits into a lower $^2P_{1/2}$ and a higher $^2P_{3/2}$ level, with a separation of 63.42 cm^{-1} (Ref. [10]). The SO interaction causes the $^2\Pi$ diatomic term to split into $^2\Pi_{1/2}$ and $^2\Pi_{3/2}$ levels, and the $^2\Sigma^+$ term becomes $^2\Sigma_{1/2}^+$; the lowest $^2\Pi_{1/2}$ level correlates to the $C^+(^2P_{1/2})$ + RG($^1S_0$) asymptote, while the $^2\Pi_{3/2}$ and $^2\Sigma_{1/2}^+$ levels both correlate to $C^+(^2P_{3/2})$ + RG($^1S_0$).

Since Ω levels of the same value can mix, an interaction between the $^2\Pi_{1/2}$ and $^2\Sigma_{1/2}^+$ levels is expected. The mixing of these is expected to be small, and so we consider the resulting $\Omega = {}^1/_2$ levels as perturbed versions of the original $^2\Pi_{1/2}$ and $^2\Sigma_{1/2}^+$ levels, and maintain these Russell-Saunders labels. In principal, additional, smaller mixings can also occur if higher energy atomic states are considered.

Previous theoretical work has not included the spin-orbit interaction, although we will be able to compare our non-SO results with those. First, we note that the $X^2\Pi$ state (and the $a^4\Sigma^-$ state) of C^+-Ne has been studied at the MP2/6-31G** level of theory by Frenking et al. [11], who reported equilibrium bond lengths and harmonic vibrational frequencies; dissociation energies were also computed at the MP4/6-311G(2df,2pd)//MP2/6-31G** level of theory. Interestingly, earlier results from the same group [12], using the complete active space self-consistent field (CASSCF) approach had concluded that both the $X^2\Pi$ and $A^2\Sigma^+$ states were unbound. These appear to be the only available values reported for this species, as the values in Ref. [13] all appear to be cited from the earlier work [11] by the same authors.

More work has been done on the C^+-Ar complex, with there being both experimental and theoretical work. First, Hillier et al. [14] used a configuration interaction (CI) approach to calculate limited potential energy curves for the $X^2\Pi$ and $A^2\Sigma^+$ states (amongst others). They reported spectroscopic constants only for the $X^2\Pi$ state, which they compared to experimentally-derived values obtained from inverting scattering results, reported in the same paper. Frenking et al. [11] reported results for C^+-Ar corresponding to the C^+-Ne ones noted above. Vibrational and rotational spectroscopic results were reported by Wong and Radom [15] at the CASSCF/6-311G(MC) level of theory with equilibrium bond lengths being reported at the higher MP3/6-311G(MC)* level (MC denotes the use of versions of the basis sets devised by Maclean and Chandler [16]); dissociation energies were also computed at the MP4/6-311+G(MC)(2df)//MP3/6-311G(MC)* level of theory. As part of a study of C^+-Ar_n complexes, Froudakis et al. [17] calculated the equilibrium bond length and binding energy of the C^+-Ar complex at the MP2 and CCSD(T) levels of theory using 6-311G* and non-standard versions of Dunning's correlation-consistent basis sets, with some augmentation by diffuse functions; additionally, the harmonic vibrational frequency was calculated at the MP2 level of theory with both types of basis set.

To our knowledge there have been no reports, experimental or theoretical, on the C^+-Kr or C^+-Xe species.

With regard to experimental work, we have already noted the scattering study reported in the paper by Hillier et al. [14]. Additionally, there has been a report on the ion mobility of C^+ in Ar from Basurto and de Urquijo [18] over a range of electric field strengths, and we shall compare our results to those data. To our knowledge, no other ion transport work on C^+ in RG, except for the work on C^+ in He discussed in Ref. [9], has been reported.

2. Computational Methodology

(a) Quantum Chemistry

Interaction potentials with and without the spin-orbit interaction have been computed for the diatomic states arising from the lowest atomic asymptotes of C^+-RG in the following manner. Energies at more than 80 internuclear separations within the range 0.8 – 50 Å were evaluated at the RCCSD(T) level of theory as implemented in MOLPRO [19,20]. Standard aug-cc-pwCVXZ [21] basis sets (X = Q, 5) were used for C, Ne and Ar, while for Kr and Xe, small-core relativistic effective core potentials (ECPs) were employed to describe the innermost electrons (ECP10MDF and ECP28MDF, respectively) and the non-ECP electrons were described with standard aug-cc-pwCVXZ-PP valence basis sets [22]. In the RCCSD(T) treatment, the 1s orbital of carbon was frozen, while for the RG atoms, we froze orbitals corresponding to 1s for Ne, 1s, 2s and 2p for Ar, 3s and 3p for Kr, and 4s and 4p for Xe, noting also the use of ECPs in the latter two cases. Interaction energies at each separation were counterpoise- (CP-) corrected to account for basis set superposition error. Finally, the CP-corrected interaction potentials were point-by-point extrapolated to the basis set limit utilising the two-point (cubic) formula of Halkier *et al.* [23,24] at each separation; these final potentials are denoted as RCCSD(T)/aV∞Z. To include the spin-orbit interaction, the CP-corrected interaction energies were used as the unperturbed eigenvalues of the Breit-Pauli spin-orbit matrix as implemented in MOLPRO to allow calculation of CP-corrected RCCSD(T) interaction energies inclusive of spin-orbit splitting at each separation, using the quadruple-ζ and quintuple-ζ basis sets as described; extrapolation of the resulting interaction energies was then performed [25].

We note that the potentials were calculated with a high precision in MOLPRO, with convergence of the energy to 10^{-12} E_h, orbitals in the SCF program to 10^{-8} and the CCSD coefficients to 10^{-7}.

Our T_1 diagnostic values [26] were < 0.05 except for C^+-Ar where the largest value was 0.071. Although these values are generally acceptable, we also undertook complete active space self-consistent field (CASSCF) followed by multireference configuration interaction (MRCI) calculations. These will be shown to confirm that multireference behaviour is not unduly affecting the values of the rovibrational spectroscopic constants, although the spin-orbit splitting of the $^2\Pi_\Omega$ states is affected and this is discussed below. MRCI calculations were undertaken using aug-cc-pwCVQZ(-PP) basis sets (aug-cc-

pVQZ for He), again employing ECP10MDF for Kr and ECP28MDF for Xe. The CASSCF+MRCI calculations used the following active spaces:

C^+-He: all electrons correlated, with an active space consisting of orbitals arising from the He 1s and C 1s2s2p atomic orbitals. Two $^2\Pi$ and one $^2\Sigma^+$ state were included in the state-averaged CASSCF calculation.

C^+-Ne: orbitals arising from C 1s and Ne 1s were frozen, while the remaining electrons were correlated in the orbitals arising from the Ne 2s2p and C 2s2p atomic orbitals. Two $^2\Pi$ and one $^2\Sigma^+$ state were included in the state-averaged CASSCF calculation.

C^+-Ar: orbitals arising from C 1s and Ar 1s2s2p were frozen, while the remaining electrons were correlated in the orbitals arising from the C 2s2p and Ar 3s3p atomic orbitals. Two $^2\Pi$ and three $^2\Sigma^+$ states were included in the state-averaged CASSCF calculation.

C^+-Kr: orbitals arising from C 1s and Kr 3s3p3d were frozen (noting the use of an ECP), while the remaining electrons were correlated in the orbitals arising from the C 2s2p and Kr 4s4p atomic orbitals. Two $^2\Pi$ and three $^2\Sigma^+$ states were included in the state-averaged CASSCF calculation.

C^+-Xe: orbitals arising from C 1s and Xe 4s4p4d were frozen (noting the use of an ECP), while the remaining electrons were correlated in the orbitals arising from the C 2s2p and Xe 5s5p atomic orbitals. Two $^2\Pi$ and three $^2\Sigma^+$ states were included in the state-averaged CASSCF calculation.

Population analyses were carried out for the $X^2\Pi$ state at the RCCSD(T)/aV∞Z R_e value using the standard Mulliken population analysis; in addition, we used the NBO program embedded in Gaussian 09 [27] to undertake a natural population analysis (NPA) for each of the complexes. Charge analyses were also undertaken with Bader's atoms-in-molecules (AIM) method, with the latter being performed with AIMAll [28]. In all cases, triple-ζ quality versions of the basis sets employed for the potential energy curves above were used, and the QCISD density (from Gaussian) was employed.

We also produced contour plots for the $^2\Pi$ state using the Hartree-Fock densities, calculated at the RCCSD(T)/aV∞Z R_e value, again using triple-ζ versions of the above basis sets.

Rovibrational energy levels were obtained from the calculated interaction potentials using the LEVEL program [29]. The lowest two relevant levels were used in each case to obtain the spectroscopic constants from standard formulae. We calculated these for $^{12}C^+$ with the most abundant naturally-occurring RG isotope in each case.

(b) Transport Coefficients

We calculated the transport cross sections for C^+ in RG from RCCSD(T) *ab initio* interaction potential energy curves as functions of the ion-neutral collision energy using the classical-mechanical program PC [30] that is an improved version of the earlier program QVALUES [31,32]. The cross sections converged within 0.05% in all cases. The range of collision energies covered was from 1×10^{-9} E_h to the energy calculated at the smallest internuclear separation: between 1.00 and 3.42 E_h, depending on the system.

The cross sections as a function of collision energy were used in the program GC [31,33,34] to determine the reduced mobility, K_0, and the other gaseous ion transport coefficients as functions of E/n_0 (the ratio of the electric field to the gas number density) at gas temperatures, T, of 100, 200, 300, 400 and 500 K for all species, and additionally at 293 K and 310 K for C^+ in Ar. The range of E/n_0 covered was 0.01–1000 Td (1 Td = 10^{-21} V m^2). We also used program VARY [35] to determine the zero-field values of the mobility and the ion diffusion coefficient as a function of T from 0.001 to 10000 K. Calculations were performed for both $^{12}C^+$ and $^{13}C^+$, while each RG was assumed to be composed of the naturally-occurring mixture of isotopes. The calculated mobilities are generally precise to within the precision of the cross sections at E/n_0 values below 20 Td. The results are progressively less precise as E/n_0 increases to 1000 Td. These details, as well as the mobilities and other transport properties, can be obtained from the tables placed in the database that is maintained from the University of Toulouse [36]. Various weightings of the cross-sections were employed for each system, and these will be stated at the appropriate points below.

Additionally, it should be noted that each spin-orbit interaction potential was shifted uniformly such that the interaction energies computed at 50 Å, were equal to the appropriate $1/R^4$ ion-induced dipole interaction energy at this separation, and then the latter potential used for all longer R values. This was done so that the transport cross sections smoothly approached the ion induced-dipole values that are correct at zero energy for the transport calculations; this shift has a negligible effect on the spectroscopic constants obtained from these potentials, but was essential for correctly calculating the zero-field mobility, especially at low T.

We ran into problems converging the transport properties for the $^2P_{1/2}$ states of C^+-RG for RG = Ar–Xe, in the region of E/n_0 between their mobility minima and maxima. We obtained estimates of the mobilities in these regions by not considering the convergence of the other transport properties and by forcing the GC program to continue until a kinetic theory approximation of at least a preselected order N. Using N values from 5 to 8 gave sets of mobilities from which we omitted occasional ones that were inconsistent with the others. For a particular RG, a polynomial curve was fitted to the remaining values from this process together with a short region of the converged values obtained by using GC in the usual

manner, and this is shown as a dotted line in each of the plots discussed below for RG = Ar, Kr and Xe. We expect these curves to be reliable to 5%.

3. Results and Discussion

(a) Spectroscopic Constants

Portions of the non-SO RCCSD(T)/aV∞Z potentials for the $X^2\Pi$ and $A^2\Sigma^+$ states, showing the potential energy minima, are shown in Figure 1 for $C^+(^2P)$-RG (RG = Ne–Xe). For each of the C^+-RG curves, the full range of values calculated are included as Supplementary Material for RG = Ne–Xe. The corresponding potential for C^+-He is available in Ref. [9]. From these plots it can be seen that the $X^2\Pi$ states are always much more strongly bound than are the $A^2\Sigma^+$ ones. This is in line with the fact that the latter have the unpaired carbon 2p electron positioned along the internuclear axis, where there will be higher electron repulsion with electrons from the RG atom. For the $^2\Pi$ state, the unpaired electron is positioned perpendicular to the internuclear axis, reducing electron repulsion, and so allowing the RG atom to interact more effectively with the positive charge on the carbon nucleus. The spectroscopic constants obtained from the non-SO interaction potentials are presented in Table 1, and these are commented on below. Additionally, we provide the calculated vibrational energy levels as Supplementary Material.

To check if multireference character may be affecting the spectroscopic parameters, we also calculated MRCI curves (although not over such a wide range as the RCCSD(T) ones) and from these derived the spectroscopic parameters. We then compared these to the non-SO non-CP-corrected RCCSD(T)/QZ results, with the sets of data presented together in Table 2 for easy comparison. As may be seen, there are small differences between the two sets of results, with the potential curves from the MRCI calculations generally tending to be very slightly deeper, except for RG = Ne, with consistent changes to the other spectroscopic parameters. Although these differences should be borne in mind, in percentage terms they are relatively small. In addition, with the use of the RCCSD(T) method we can use larger basis sets than for CASSCF+MRCI, there is less worry about the size of the active space, and it is more practicable to include the counterpoise correction to correct for basis set superposition error. Further, we note the very good agreement of the present RCCSD(T)/aV∞Z values with the only spectroscopic parameters that have been determined experimentally, from the scattering experiments in Ref. [14] for C^+-Ar is very good – see below.

(b) Comparison with previous results

Here we shall compare our non-SO RCCSD(T) results to previous theoretical results, as the present study is the first to include SO effects. All of the present and previous results have been summarized in Table 1.

With regard to C^+-Ne, it is clear that the earlier CASSCF results from Koch and Frenking [12], which concluded the species was unbound, are not in line with later results from the same group [11], nor with those here. Taken together, these results suggest that dynamic electron correlation is an important consideration in these species. The agreement between the MP2/6-31G** results of Ref. [11] and those here is reasonably good, although the harmonic vibrational frequency and R_e values from that work suggest a more strongly-bound species, while the MP4 D_e value suggests it is slightly weaker. Overall, the present results are more consistent and expected to be the more reliable. Unfortunately there are no experimental values with which to compare.

For C^+/Ar, scattering experiments [14] have led to various spectroscopic values being derived from a potential obtained from inverting the scattering data; the agreement between those values and ours is very good overall. (We note in passing that the B_e values reported in that work are not consistent with the R_e values they report: we have put corrected values in Table 1.) In Ref. [14] the C^+ ions were produced either by a plasma ion source or electron bombardment and so it is not completely clear whether the ^2P ions are in the $^2P_{1/2}$ ground level, a statistical mix of the two spin-orbit levels, or something in between. In any case, only a single potential energy curve was reported following inversion of the scattering data, and was simply referred to as a $^2\Pi$ state in that work. Given the similarity of the spectroscopic parameters for the $^2\Pi$ term and the two $^2\Pi_\Omega$ levels, we would expect similar results from inverting either of these experimental populations.

The configuration interaction (CI) potential generated in Ref. [14] for the $^2\Pi$ state of C^+-Ar appears to be too deep, and although the R_e value is similar to that calculated here, the ω_e value is significantly higher. Detailed spectroscopic results were not reported for the $^2\Sigma^+$ state, but an R_e value of ~ 3.0 Å can be deduced from the tabulated potential energy data; this value is in good agreement with the present value.

The C^+-Ar parameters from Frenking et al. [11] suggest that that their MP2/6-31G** calculations are underestimating the interaction strength overall for the $^2\Pi$ state; no results for the $^2\Sigma^+$ state were reported. Wong and Radom [15] reported CASSCF calculations that suggest a dramatic underestimation of the well depth (consistent with the results from Ref. [12] on C^+-Ne commented on above), while the MP3 results are in better agreement with the D_e value, and the MP4 values even more so; even the latter are somewhat below the present RCCSD(T) results. Again, these observations are consistent with dynamic electron correlation being of great importance in describing the interactions in these species reliably. Thus, the present results are expected to be the most reliable.

Finally, we comment on the C^+-Ar results from Froudakis et al. [17] who used the MP2 and CCSD(T) approaches. They used 6-311G* basis sets, augmented with diffuse functions in the case of Ar, as well as aug-cc-pVDZ basis sets, again augmented with diffuse functions in the case of Ar. (Although not

explicitly stated, we assume unrestricted calculations were undertaken.) It may be seen that the MP2 results are in good agreement with respect to the R_e value, but the interaction energy is significantly lower. The results at the CCSD(T) level, however, including ω_e, are in much better agreement – again confirming the importance of dynamic correlation energy.

We note that the present values for C^+-Kr and C^+-Xe appear to be the only ones available either experimentally or theoretically.

(c) Effect of spin-orbit coupling

We now turn to examining the effect of inclusion of the spin-orbit interaction. First, referring to Figure 1, we note that with no spin-orbit coupling, the $^2\Pi$ and $^2\Sigma^+$ states that arise from the $1s^22s^22p^1$ electronic configuration of C^+ after interaction with RG occurs, converge to the same asymptote. After spin-orbit coupling is turned on, then in terms of the atomic spin-orbit coupling constant, ζ, there are two atomic asymptotes: $C^+(^2P_{3/2})$ + RG($^1S_0$) at $+\zeta/2$ and $C^+(^2P_{1/2})$ + RG($^1S_0$) at $-\zeta$, where ζ is the spin-orbit coupling constant for C^+.

In Figure 1, we also show the result of spin-orbit coupling on the diatomic curves. As indicated above, there are two main effects of spin-orbit coupling, which happens simultaneously. First, the $^2\Pi$ state splits into $^2\Pi_{1/2}$ and $^2\Pi_{3/2}$ states, with the former state being the lower by Hund's rules. Secondly, the $^2\Pi_{1/2}$ and $^2\Sigma_{1/2}{}^+$ states interact, with this interaction depending on the energetic separation of the two states [37]. Further, both the $^2\Pi_{3/2}$ and $^2\Sigma_{1/2}{}^+$ states converge to the upper asymptote, with the $^2\Pi_{1/2}$ one converging to the lower one. (The requirement for the curves to converge to a particular spin-orbit asymptote is also manifested in this mixing of the $^2\Pi_{1/2}$ and $^2\Sigma_{1/2}{}^+$ states.) In the absence of any other effects, we expect Hund's case (a) coupling to apply, and so the $^2\Pi_{1/2}$–$^2\Pi_{3/2}$ spacing to be ζ, where $^3/_2\zeta$ is the asymptotic $^2P_{1/2}$–$^2P_{3/2}$ splitting of C^+; further, because we expect the SO interaction in this diatomic system to be small, it is acceptable to maintain the unmixed Hund's case (a) labels for each state. (We have discussed the evolution from Hund's case (a) to Hund's case (c) in Ref. [37] in the case where the interactions are localized to a …p^1 configuration.)

In Table 3 we report the spin-orbit splittings calculated at the R_e values of the respective species and compare these to the calculated splitting at the asymptote. First, we note that the asymptotic splittings are all the same, as expected, since these will be solely that for the isolated C^+ cation. The experimental asymptotic splitting is $^3/_2\zeta$ = 63.42 cm^{-1} [38] and this can be very favourably compared with the present calculated value of 61.2 cm^{-1}. What is very interesting is the variation in the $^2\Pi_{1/2}$–$^2\Pi_{3/2}$ splitting. For RG = He and Ne, this has a value of ζ, within experimental error, implying that Hund's case (a) coupling applies, as expected for a light atom such as carbon. However, there is a rapid rise in the $^2\Pi_{1/2}$–$^2\Pi_{3/2}$ splittings as we move through the other C^+-RG species, far in excess of any reasonable deviation from

Hund's case (a) coupling, and indeed the values are greater than the atomic splittings; thus, we sought another explanation for this. One such explanation would be small amounts of charge transfer since the ionization energy of the RG atom is decreasing with increasing atomic number. We note that for Xe the ionization energy (12.13 eV [38]) is very close to that of C (11.260 eV [38]). This charge transfer may be viewed as mixing in small amounts of C-RG$^+$ character into the C$^+$-RG wavefunctions; note that only small amounts of mixing would be required to explain the results, since the spin-orbit splitting rises approximately as the fourth power of the atomic number – see Table 3. We investigated this hypothesis using our MRCI calculations, reported above, with the coefficients being presented in Table 4. These indicate that there is a small increase in the amount of C-RG$^+$ character with a concomitant drop off in the C$^+$-RG character as the atomic number of RG increases. Thus, the charge-transfer hypothesis appears to be sound and explains the observed results. There are a few points to note, however. First, there was a very small amount of mixing of other states in the MRCI wavefunction, but this does not change the overall conclusion regarding charge transfer. Secondly, it might be questioned as to how the charge transfer was present in the RCCSD(T) wavefunction, which is ostensibly a single-reference method. Regarding the latter, the ability of the CCSD(T) approach to perform well even when there are small amounts of multireference character has been discussed a number of times - see, for example Ref. [39].

The change in shapes of the curves is evident in Figure 1, and it is also instructive to look at the difference between the spectroscopic constants recorded with and without the spin-orbit interaction – see Table 1. First, for C$^+$-He and C$^+$-Ne we note that the values for the $^2\Pi$ terms and the $^2\Pi_{3/2}$ level are all extremely similar, as expected, since there are no other Ω = 3/2 states with which to interact. In contrast, differences are expected in the $^2\Sigma_{1/2}{}^+$ and $^2\Pi_{1/2}$ curves since there will be mixing between these. The effect on the spectroscopic parameters will be *R* dependent because it depends on the energy separation at each point [37], but a general conclusion is that the $^2\Pi_{1/2}$ state becomes slightly more weakly bound, while the $^2\Sigma_{1/2}{}^+$ state becomes slightly more strongly bound. The separation between the $^2\Pi_{1/2}$ and $^2\Pi_{3/2}$ states gives some insight into the nature of the spin-orbit coupling: for a pure Hund's case (a) we expect a splitting of ζ, while for pure Hund's case (c) we expect $^3/_2\zeta$. This splitting is given in Table 3, where we can see that these two lightest complexes have splittings that are commensurate with Hund's case (a).

For C$^+$-Ar, again the spectroscopic parameters from the $^2\Pi$ term and the $^2\Pi_{3/2}$ level are very similar, but now we see that the value of the $^2\Pi_{1/2}$–$^2\Pi_{3/2}$ splitting of 1.47ζ. Although this is very close to that expected for pure Hund's case (c) coupling, this is thought to be coincidental – see next paragraph.

It is interesting that for C$^+$-Kr and C$^+$-Xe, there are more marked differences between the values of the spectroscopic parameters for the $^2\Pi$ term, and *both* the $^2\Pi_{1/2}$ and $^2\Pi_{3/2}$ levels. We have noted above that

the $^2\Pi_{1/2}$–$^2\Pi_{3/2}$ splittings are significantly above even Hund's case (c) splitting for the heaviest two species and this suggests that other factors have come into play – this is again evidence for the mixing in of C-RG$^+$ character discussed above, where the $^2\Pi_{3/2}$ state is no longer a pure π state. The MRCI calculations are consistent with this, and also suggest that the $^2\Pi_{1/2}$–$^2\Pi_{3/2}$ splitting in C$^+$-Ar being close to the Hund's case (c) value is coincidental.

We note that this involvement of the RG orbitals has been observed in excited states of M$^+$-RG complexes [40], and this has been considered by both Duncan and coworkers [41], and Breckenridge and coworkers [42] in their electronic spectroscopic study of Mg$^+$-RG complexes.

(d) Trends in the spectroscopic constants

In Figure 2 we show trends in four spectroscopic quantities as the atomic number of the rare gas atom increases. We plot the values from the non-SO RCCSD(T)/aV∞Z calculations from the present work for RG = Ne–Xe, with the corresponding C$^+$-He values being taken from Ref. [9].

For R_e, there is an initial decrease going from He to Ar for the $^2\Pi$ state suggesting that the increasing polarizability is allowing the RG atom to get closer despite its increasing size; however, this reverses thereafter, suggesting the increasing size starts to dominate. For the $^2\Sigma^+$ state we have the reverse trend, suggesting a dominance of the electron repulsion, owing to the location of the unpaired electron on the carbon ion being along the internuclear axis. The subsequent fall in R_e is likely related to small hybridization effects allowing movement of electron density away from the incoming RG atom whose cost is offset by the stronger interaction with the more polarizable Kr and Xe atoms, as they move closer and so interact more strongly.

For D_e, we see that these are monotonically increasing for both states, but significantly more steeply for the $^2\Pi$ state. This is consistent with the increasing polarizability of the RG atom, plus the reduced electron repulsion in the $^2\Pi$ state compared to the $^2\Sigma^+$ one.

We can see that the trends in ω_e and k are quite similar, so that the mass effect in ω_e does not alter the overall trend dramatically. Additionally, the trend in k is also monotonically increasing, and so is consistent with the D_e trend.

(e) Chemical bonding effects?

In Figure 3 we show contour plots of the Hartree-Fock electron density for the highest-occupied molecular orbital (HOMO) for the X$^2\Pi$ state of each C$^+$-RG species (RG = He–Xe), each calculated at the RCCSD(T)/aV∞Z (no SO) R_e value. For C$^+$-He there is very little sharing of electron density across the centres and we can say that the interactions are almost entirely physical. However, as we move

towards the heavier rare gases the HOMO has a small but significant contribution from the off-axis, outermost occupied p orbitals on the RG centre, suggesting a small amount of chemical interaction.

Another way of examining this is via charge/population analysis, and the results for this are presented in Table 5; these are performed on the QCISD/aVQZ electron density. Here we have presented Mulliken, NPA and AIM charges. In line with expectations from some of our previous work [43], we find that the Mulliken charges are unphysical in that they suggest close to a complete electron transfer for C^+-Xe, with very significant transfers also occurring for C^+-Ar and C^+-Kr; this is in contrast to the spin densities, which show an unpaired electron to be located on the carbon centre. The NPA and AIM charges are more reasonable for C^+-Xe, but surprisingly similar to the Mulliken charges for the other C^+-RG species. Our conclusion is that although these methods are consistent with some charge transfer occurring between the carbon cation and the rare gas atom, the amount seems unphysical: certainly it is not consistent with the MRCI analysis, nor with the calculated $^2\Pi_{1/2}$–$^2\Pi_{3/2}$ spin-orbit gaps (these would be very much higher if such a significant charge transfer had occurred – see Table 3). We tested the stability of these results by using small 6-31G* basis sets for C^+-Ar, but obtained charges that were within 0.02*e* for the Mulliken and NPA approaches, and within 0.05*e* for AIM, when compared to the results in Table 5.

Another measure of the extent of chemical bonding is the $H(R)$ parameter [44], which is indicative of chemical bonding if it is negative. Table 5 shows that the values are all very small, but that those for C^+-Ar, C^+-Kr and C^+-Xe are consistent with a small amount of chemical bonding.

Finally, we examine Birge-Sponer plots from the calculated vibrational energy spacings, and present these in Figure 4. As may be seen, the $^2\Pi$ plots do not all simply consist of a linear portion together with a long-range "tail", as would be expected for a molecular complex, and as is seen for the $^2\Sigma^+$ ones. On the $^2\Pi$ plots, we have used our derived values of ω_e and $\omega_e x_e$ (Table 1) to plot an "ideal" Birge-Sponer line, recalling that the values in Table 1 are obtained from the lowest two vibrational energy levels, as well as the D_e value. As may be seen, this line is close to fitting all but one of the C^+-He points, and does a good job of fitting the first eight or so points for C^+-Ne, before the long-range tail takes over. However, for the heavier three species (RG = Ar–Xe), this line only fits a portion of the lowest-*v* values. Closer examination of these curves, reveals that there is actually a second linear section of data just before the long-range tail (indicated with filled-in circles on the plots) before the slope gradually evolves into the shallower slope that occurs close to $v = 0$; if this were analysed (which is difficult to do as the extent of the linear region is difficult to define unambiguously) it would lead to a higher ω_e value than that obtained from the lowest *v* values, i.e. close to the minimum. This suggests that the potential is "softer" close to R_e than it is just before the long-range tail region at high-*v* values. A clue to the interpretation of this observation comes from the contour plots in Figure 3. These show that the off-axis orbitals on the carbon and RG centres are distorted away from each other. We

hypothesise that the softening of the potential as R_e is approached occurs from increased short-range repulsion which softens the form of the overall (repulsion+attraction) potential in the $^2\Pi$ state. The fact that the Birge-Sponer plots change their character as a function of v could be taken as further evidence for "chemical" contributions (via distortion of electron density) to the interaction potential for the $^2\Pi$ state.

The Birge-Sponer plots for the $^2\Pi$ state are in contrast to those of the $^2\Sigma^+$ state, which are also shown in Figure 4. Although there are generally fewer levels, there are still enough to demonstrate that the behaviour here is "normal" with a linear region at low-v and a long-range tail to high v, with only a slight deviation for C^+-Xe. This is in line with there being no off-axis electron density on the carbon centre to cause the additional repulsion close to R_e as discussed above for the $^2\Pi$ state.

(f) Transport coefficients

We shall now discuss the calculation of ion transport coefficients using the RCCSD(T) potentials. In all cases, we shall only discuss the results for $^{12}C^+$ here, although results for $^{13}C^+$ have also been calculated and are reported in the Toulouse database [36]. In all cases, for each RG we assumed a mixture of isotopes was present with their naturally-occurring abundances. Since experimental results are only available for C^+ in Ar, we discuss this system first, and then briefly discuss the results for C^+ in Ne, Kr and Xe afterwards. (As noted above, a detailed discussion of the mobility of C^+ in He, compared to available experimental data was presented in Ref. [9].)

i. $C^+(^2P)$ with argon

Ion mobilities, diffusion coefficients and other transport properties have been calculated from both the non-SO and the SO potentials arising from the lowest doublet states of C^+ interacting with argon. These are computed over a wide range of E/n_0 and at a variety of temperatures, including those at which experimental data [18] have been taken. Although ground, statistical and excited state weightings were used for the field-dependent and zero-field calculations, we only present the values for selected states or mixtures thereof, with the full dataset being available in the Toulouse database [36].

Cross-sections were calculated from each potential curve, and then various weightings of these were employed in generating the transport data to compare with experiment, since the actual ionic state populations are not definitively known owing to: the ion production method; uncertainty regarding thermalization; injection effects; and the effect of the collisions during the ion drift region. The weightings chosen were those of the ground state (100% $^2\Pi$ or 100% $^2\Pi_{1/2}$ cross-sections), the excited state (100% $^2\Sigma^+$ or a 1:1 weighting of the $^2\Pi_{3/2}$ and $^2\Sigma_{1/2}{}^+$ cross-sections) and a statistical mixture (2:1 weighting of $^2\Pi$ and $^2\Sigma^+$ or a 1:1:1 weighting of $^2\Pi_{1/2}$, $^2\Pi_{3/2}$ and $^2\Sigma_{1/2}{}^+$ cross-sections). A portion of the results are presented in Figure 5 together with the experimental data.

The conclusions from the calculations are that the experiment must have generated the $^2P_{1/2}$ ground spin-orbit level. In previous work [9,45,46] we have concluded that the experiment conditions can affect the mix of spin-orbit states owing to incomplete thermalization; in such cases the ions were generally produced in a very energetic source, such as electron bombardment. In the present case the results in Figure 5 are fairly conclusive that only the $^2P_{1/2}$ state is populated to any great extent in the experiment. The possibility of different states being present was not considered in Ref. [18]; we hypothesise that the presence only of the lower spin-orbit level arises from the ion production method in that work, namely charge transfer via collision of Ar with CF_3^+ and at reasonable pressures that allow collisional deactivation of any excited states.

Often, the temperatures employed for ion mobility measurements can be critical in obtaining reliable values. In Ref. [18], the temperature was maintained only within a 17 K range 293–310 K, and so we calculated mobilities at the upper and lower limits. As it happens, within the uncertainties in the experimental measurements, it was not possible to differentiate between these results.

ii. C^+ in RG (RG = Ne, Kr,Xe)

No experimental data exists for C^+ in the other three RG, but for completeness we have calculated transport data for them at a range of temperatures and archived the results in the Toulouse database [36]. Here we simply show a summary of the mobilities for C^+ in each of the four RG gases (Ne–Xe) in Figure 5.

iii. Zero-field mobilities

In Figure 6 we have plotted the zero-field mobilities as a function of T for the $^2P_{1/2}$ state. These are the mobilities obtained when $E/n_0 \rightarrow 0$ and as such are directly proportional to the zero-field ion diffusion coefficients, D, according to the Nernst-Townsend-Einstein relation [47]; as a consequence the D values for any system can be obtained from the zero-field mobility values (and *vice versa*) – however, the values are all available from the Toulouse database [36].

As may be seen from Figure 6, the variation of K_0 with T is slow at low values, but the gas temperature must be extremely small before K_0 is equal to the polarization mobility that can be determined from the ion-neutral reduced mass and the electric dipole polarizaibility, α, of the neutral. If only moderate accuracy is required, then the zero-field mobility can be used in analyzing experiments below and near room temperature, but it is important to establish that one is working in the zero-field region, which can be estimated from an expression given in Ref. [48]; for more accurate results the E/n_0 dependence must be included. These issues have been discussed in detail recently [49].

In passing, we note that in Ref. [18] an incorrect value for the electric dipole polarizability of Ar was used. Correcting this gives a theoretical zero-field mobility of 3.558 $cm^2\,V^{-1}\,s^{-1}$, which is outside the range of 3.40±0.08 $cm^2V^{-1}s^{-1}$ reported in Ref. [18], and more in line with discrepancies they saw for other measurements. As a consequence, the surprise they noted at the good agreement in the case of C^+ in Ar was unwarranted.

4. Concluding Remarks

In the present work, we have calculated very accurate potential energy curves for the interaction of C^+ with RG (RG = Ne–Xe), which complements our earlier work on C^+ interacting with He [9]. For the first time, we have investigated the effect of spin-orbit coupling, which has revealed a small amount of charge transfer in the C^+-RG complexes. We have used these potentials to calculate reliable values for a range of spectroscopic constants and examined the effects of spin-orbit coupling on these. Consideration of wavefunction contour plots and Birge-Sponer plots led to the conclusion that there was a small amount of chemical interaction in these species for RG = Ar–Xe, which is consistent with the implications of the spin-orbit splittings. Although these conclusions were consistent with the values of $H(R)$ and the spin density, we found that Mulliken, NPA and AIM charges suggested anomalously high amounts of charge transfer.

We have also calculated transport coefficients and compared the calculated ion mobilities to experiment in the case of C^+ in Ar – the only case for which experimental data was available. The results indicated that predominantly the ground $^2P_{1/2}$ state was present in the experiments. We have calculated a range of other properties, including zero-field mobilities and diffusion coefficients and these should prove useful in ion-molecule kinetics experiments.

Acknowledgements

TGW, WDT and RLT are grateful for the provision of computing time by the EPSRC under the auspices of the NSCCS, and are also grateful for access to the University of Nottingham High Performance Computing Facility. The EPSRC are thanked for the provision of a studentship to W.D.T.

Author Contributions

TGW conceived and supervised the research and wrote the manuscript. WDT performed quantum chemistry calculations, undertook analyses, commented on drafts of the manuscript and approved the final version. RLT performed quantum chemistry calculations, undertook analyses and approved the final version. LAV performed the transport coefficient calculations, commented on drafts of the

manuscript and approved the final version. WHB provided insight into the analyses, commented on drafts of the manuscript and approved the final version.

Competing Interests. The authors declare that they have no competing interests.

Figure Captions

Figure 1: Potential energy curves calculated for C^+ interacting with RG. The legend in the first panel applies to all plots. The interaction energies have been calculated at the RCCSD(T)/aV∞Z level of theory and both non-SO and SO curves are shown as dashed and solid lines, respectively – see text for details. The zoom-ins in three of the plots have the same vertical energy scale and similar to that in the C^+-Ne plot, allowing visual comparison of the evolution of the spin-orbit splitting of the $^2\Pi_\Omega$ states as the atomic number of the RG atom increases.

Figure 2: Trends in various spectroscopic parameters as a function of RG. See text.

Figure 3: Contour plots of the highest occupied molecular orbitals (HOMOs) for the $X^2\Pi$ state of each of the C^+–RG systems (RG = He–Xe) calculated at the R_e value derived at the RCCSD(T)/aV∞Z level. See text for discussion.

Figure 4: Birge-Sponer plots constructed from the calculated vibrational energy spacings obtained from the RCCSD(T)/aV∞Z potentials. The solid lines are obtained from the ω_e and $\omega_e x_e$ values reported in Table 1 and come from the lowest two vibrational energy levels and D_e. For the $^2\Pi$ state, the filled circles indicate levels at high v that form a linear section of the plot close to the long-range region.

Figure 5: Calculated K_0 versus E/n_0 for C^+ in RG at the indicated temperatures presented as semilog plots. In all plots, the values for solely $^2P_{1/2}$ and solely $^2P_{3/2}$ states are given, as well as a statistical mix of the two – the legend in the first panel applies to all plots. In addition, for RG = Ar we have included the experimental mobilities reported in Ref. [18], where T varied between 293 K and 310 K, together with error bars consistent with that work. For RG = Ar, Kr and Xe, we indicate the region for which convergence problems were obtained by a dotted line; the data within these ranges is less reliable than the rest – see text.

Figure 6: Calculated zero-field mobilities versus T for the $^2P_{1/2}$ state of C^+-RG presented as a log-log plot. The polarization limit is given in each case at the left-hand side of the plot.

Table 1: Spectroscopic constants for $^{12}C^+(^2P_J)$-RG($^1S_0$) (RG = He – Xe).

State	R_e (Å)	D_e (cm^{-1})	D_0 (cm^{-1})	ω_e (cm^{-1})	$\omega_e x_e$ (cm^{-1})	k (N m^{-1})	B_e (cm^{-1})	α	Source[a]
C^+-He									
$^2\Pi_{1/2}$	2.201	456.3	368.5	185.5	19.67	6.083	1.159	1.33×10^{-1}	[9][b]
$^2\Pi_{3/2}$	2.200	476.2	388.0	186.0	19.07	6.120	1.160	1.31×10^{-1}	[9][b]
$^2\Pi$ (non-SO)	2.200	476.1	387.9	186.0	19.07	6.120	1.160	1.32×10^{-1}	[9][b]
$^2\Sigma_{1/2}^+$	2.946	135.5	93.9	92.45	18.43	1.512	0.647	1.27×10^{-1}	[9][b]
$^2\Sigma^+$ (non-SO)	2.968	121.8	83.3	85.88	17.83	1.304	0.638	1.36×10^{-1}	[9][b]
C^+-Ne									
$^2\Pi_{1/2}$	2.146	1122.7	1028.4	192.8	8.60	16.418	0.488	2.38×10^{-2}	Present work
$^2\Pi_{3/2}$	2.146	1142.5	1048.2	192.8	8.58	16.431	0.488	2.39×10^{-2}	Present work
$^2\Pi$ (non-SO)	2.146	1142.7	1048.4	192.9	8.58	16.432	0.488	2.38×10^{-2}	Present work
	unbound								[12][c]
	2.077	1050	940	222					[11][d]
$^2\Sigma_{1/2}^+$	2.958	259.6	221.7	79.4	7.25	2.784	0.257	2.21×10^{-2}	Present work
$^2\Sigma^+$ (non-SO)	2.965	242.7	206.0	77.1	7.56	2.628	0.256	2.34×10^{-2}	Present work
C^+-Ar									
$^2\Pi_{1/2}$	1.996	7971.5	7765.8	413.3	4.17	92.902	0.458	5.52×10^{-3}	Present work
	1.995	7570		417	6.0		0.459	9.2×10^{-3}	Scattering [14][e]
$^2\Pi_{3/2}$	1.997	7972.6	7767.2	413.0	4.18	92.730	0.458	5.98×10^{-3}	Present work
$^2\Pi$ (non-SO)	1.996	7982.2	7776.7	413.2	4.17	92.814	0.458	6.21×10^{-3}	Present work
	2.000	9520		485	6.5		0.457	8.3×10^{-3}	[14][f]
	2.059	7210	7070	302					[11][d]
	2.114	2600		304	12.7		0.41	1.47×10^{-2}	[15][g]
	2.036	5700							[15][h]
		7500	7400						[15][i]
	2.016	6100		392					[17][j]
	2.027	6200							[17][k]
	2.001	7800		410					[17][l]
	2.004	8100							[17][m]
$^2\Sigma_{1/2}^+$	2.999	941.9	884.4	117.2	4.22	7.472	0.203	7.65×10^{-3}	Present work
$^2\Sigma^+$ (non-SO)	3.000	922.0	864.6	117.0	4.26	7.449	0.203	7.53×10^{-3}	Present work
	3.0[n]								[14][f]
C^+-Kr									
$^2\Pi_{1/2}$	2.071	11866.0	11648.3	436.8	3.10	118.012	0.374	3.54×10^{-3}	Present work
$^2\Pi_{3/2}$	2.077	11754.6	11538.5	433.7	3.07	116.335	0.372	3.90×10^{-3}	Present work
$^2\Pi$ (non-SO)	2.074	11818.3	11601.5	435.1	3.09	117.121	0.373	3.78×10^{-3}	Present work
$^2\Sigma_{1/2}^+$	2.904	1583.1	1512.2	143.6	3.94	12.760	0.190	5.46×10^{-3}	Present work
$^2\Sigma^+$ (non-SO)	2.904	1562.7	1491.9	143.6	3.95	12.750	0.190	5.47×10^{-3}	Present work
C^+-Xe									
$^2\Pi_{1/2}$	2.195	17211.4	16985.2	453.8	2.58	133.445	0.318	2.65×10^{-3}	Present work
$^2\Pi_{3/2}$	2.208	16823.9	16601.7	445.6	2.53	128.677	0.314	2.93×10^{-3}	Present work
$^2\Pi$ (non-SO)	2.202	17011.5	16787.5	449.3	2.56	130.809	0.316	2.60×10^{-3}	Present work
$^2\Sigma_{1/2}^+$	2.805	3449.0	3341.3	217.2	3.55	30.567	0.195	3.21×10^{-3}	Present work
$^2\Sigma^+$ (non-SO)	2.803	3433.7	3326.0	217.2	3.54	30.581	0.195	3.31×10^{-3}	Present work

a Appropriate reference number, method or results from the present work.

[b] RCCSD(T)/aV∞Z results [9].

[c] CASSCF calculations with a triple-ζ basis set [12].

[d] MP2/6-31G** calculations, with single-point MP4(SDTQ)/6-311G(2df,2pd) calculations for dissociation energies [11].

[e] Results from a potential obtained by inverting scattering data [14] – see text.

[f] CI results using [7s5p1d/5s3p1d] basis sets for Ar/C^+, respectively.

[g] CASSCF/6-311G(MC)* calculations [15].

[h] MP3/6-311G(MC)* calculations [15].

[i] MP4/6-311+G(MC)(2df)//MP3/6-311G(MC)* calculations [15].

[j] MP2/6-311G* calculations, with diffuse functions on Ar [17].

[k] CCSD(T)/6-311G* calculations, with diffuse functions on Ar [17].

[l] MP2/aug-cc-pVDZ calculations, with diffuse functions on Ar [17].

[m] CCSD(T)/aug-cc-pVDZ calculations, with diffuse functions on Ar [17].

[n] Estimated from tabulated potential energy values given in Ref. [14].

Table 2: Comparing MRCI and CCSD(T), R_e, D_e and ω_e

Method[a]	R_e (Å)	D_e (cm^{-1})	ω_e (cm^{-1})
C^+-He			
$^2\Pi$ CCSD(T)/QZ	2.207	464.7	185.1
$^2\Pi$ MRCI/QZ	2.197	473.0	186.4
$^2\Sigma^+$ CCSD(T)/QZ	2.984	119.8	83.8
$^2\Sigma^+$ MRCI/QZ	2.981	121.2	84.5
C^+-Ne			
$^2\Pi$ CCSD(T)/QZ	2.155	1093.8	187.0
$^2\Pi$ MRCI/QZ	2.158	1049.8	180.3
$^2\Sigma^+$ CCSD(T)/QZ	2.983	246.9	76.3
$^2\Sigma^+$ MRCI/QZ	2.995	238.6	74.9
C^+-Ar			
$^2\Pi$ CCSD(T)/QZ	2.003	7876.4	408.1
$^2\Pi$ MRCI/QZ	1.999	8024.9	413.1
$^2\Sigma^+$ CCSD(T)/QZ	3.009	901.5	115.8
$^2\Sigma^+$ MRCI/QZ	2.997	1006.2	120.9
C^+-Kr			
$^2\Pi$ CCSD(T)/QZ	2.079	11772.1	432.8
$^2\Pi$ MRCI/QZ	2.082	12042.8	434.5
$^2\Sigma^+$ CCSD(T)/QZ	2.912	1543.9	142.1
$^2\Sigma^+$ MRCI/QZ	2.910	1703.1	147.2
C^+-Xe			
$^2\Pi$ CCSD(T)/QZ	2.206	17059.3	447.4
$^2\Pi$ MRCI/QZ	2.215	17417.3	444.8
$^2\Sigma^+$ CCSD(T)/QZ	2.803	3451.6	218.1
$^2\Sigma^+$ MRCI/QZ	2.797	3783.2	223.0

[a] Where QZ indicates the use of aug-cc-pwCVQZ(-PP) basis sets for carbon and neon through xenon, with ECP10MDF for Kr and ECP28MDF for Xe. For helium, the aug-cc-pVQZ basis set was used.

Table 3: Spin-orbit parameters for C^+-RG

Parameter	**C^+-He**	**C^+-Ne**	**C^+-Ar**	**C^+-Kr**	**C^+-Xe**
Calculated asymptotic splitting (= $^3/_2\ \zeta$)[a]	61.2	61.2	61.2	61.2	61.2
Predicted calculated Hund's case (a) splitting at R_e (= ζ)[a,b]	40.8	40.8	40.8	40.8	40.8
Calculated $^2\Pi_{1/2}$-$^2\Pi_{3/2}$ splitting at R_e	41.3	41.4	60.1	172.6	448.7
Actual/Predicted splitting [c]	1.01	1.01	1.47	4.23	11.00
IE(RG)/ eV[d]	24.587	21.565	15.760	14.000	12.130
$^2P_{3/2}$–$^2P_{1/2}$ Splitting (RG^+)[d]	n/a	780.4	1431.6	5370.10	10537.01

[a] ζ is the spin-orbit splitting parameter for C^+.

[b] Predicated from the calculated asymptotic splitting.

[c] This is the ratio of the actual calculated $^2\Pi_{1/2}$–$^2\Pi_{3/2}$ splitting to the predicted Hund's case (a) splitting.

[d] From Ref. [38]: these are the first ionization energies of RG, and the spin-orbit splitting for the lowest ^2P term; there is no such term from the ground state configuration of He.

Table 4: MRCI Coefficients (C_i^2) for C^+-RG ($X^2\Pi$) at R_e [a]

Description	He	Ne	Ar	Kr	Xe
Reference state (unpaired 2p electron on C)	0.934	0.912	0.840	0.830	0.811
$1e^-$ charge transfer RG (np$_z$ → C 2p$_z$)	n/a	<0.01	0.029	0.035	0.039
$2e^-$ charge transfer RG (np$_z$ → C 2p$_z$)	n/a	<0.01	0.010	0.011	0.013

[a] Single-point CASSCF+MRCI/aVQZ calculations carried out at the R value corresponding to the lowest calculated energy – see text for further details. Only the three main contributions are shown, other small contributions were present for each species; n/a indicates that the excitation does not exist.

Table 5: Calculated charges, spin density and $H(R)$ values.[a]

RG	q(C)	q(RG)	Spin density	$H(R)$
He	(1.001) [0.990] 0.991	(-0.001) [0.010] 0.009	(0.999)	0.0025
Ne	(0.955) [0.969] 0.970	(0.045) [0.031] 0.030	(0.999)	0.0025
Ar	(0.571) [0.666] 0.708	(0.429) [0.334] 0.292	(1.002)	-0.0449
Kr	(0.534) [0.530] 0.570	(0.466) [0.470] 0.430	(1.013)	-0.0460
Xe	(0.096) [0.343] 0.380	(0.904) [0.657] 0.620	(1.024)	-0.0466

[a] Values in parentheses are from Mulliken population analysis; values in square brackets from natural population analysis (NPA) and the lone values are from Bader's atoms-in-molecules (AIM) approach – see text for further details and comments.

Figure 1

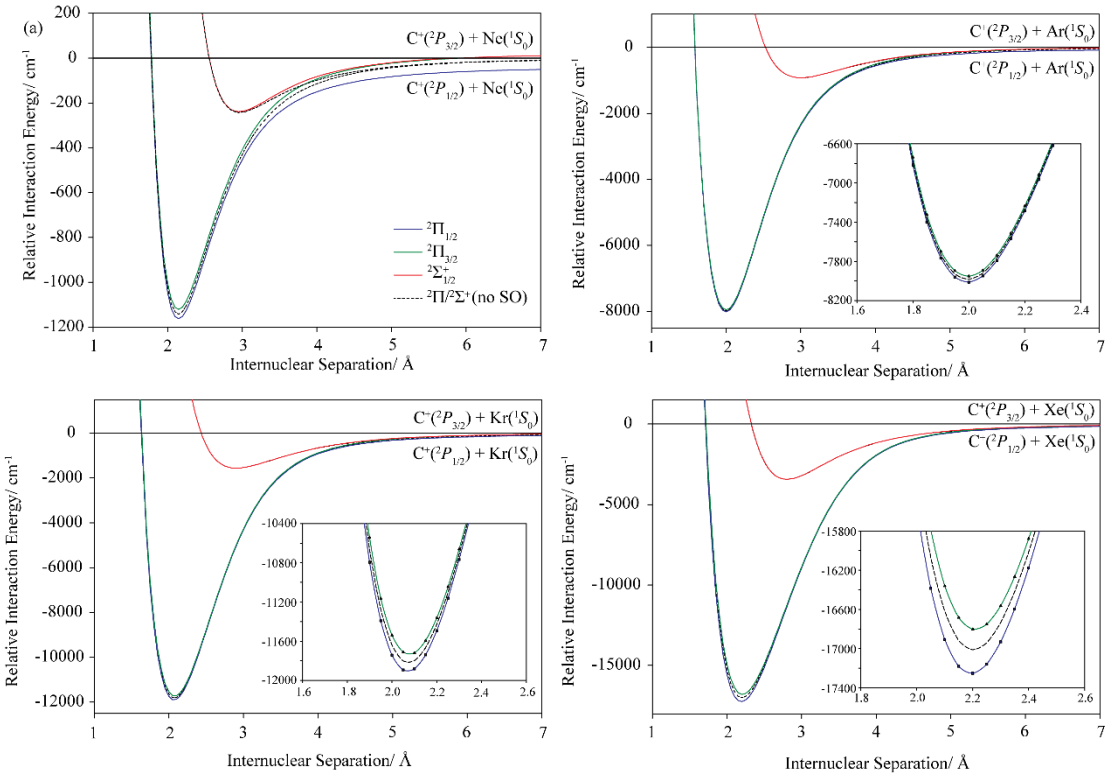
(a)
Relative Interaction Energy/ cm-1
Internuclear Separation/ Å
C+(2P3/2) + Ne(1S0)
C+(2P1/2) + Ne(1S0)
2Π1/2
2Π3/2
2Σ+1/2
2Π/2Σ+(no SO)
C+(2P3/2) + Ar(1S0)
C+(2P1/2) + Ar(1S0)
C+(2P3/2) + Kr(1S0)
C+(2P1/2) + Kr(1S0)
C+(2P3/2) + Xe(1S0)
C+(2P1/2) + Xe(1S0)

Figure 2

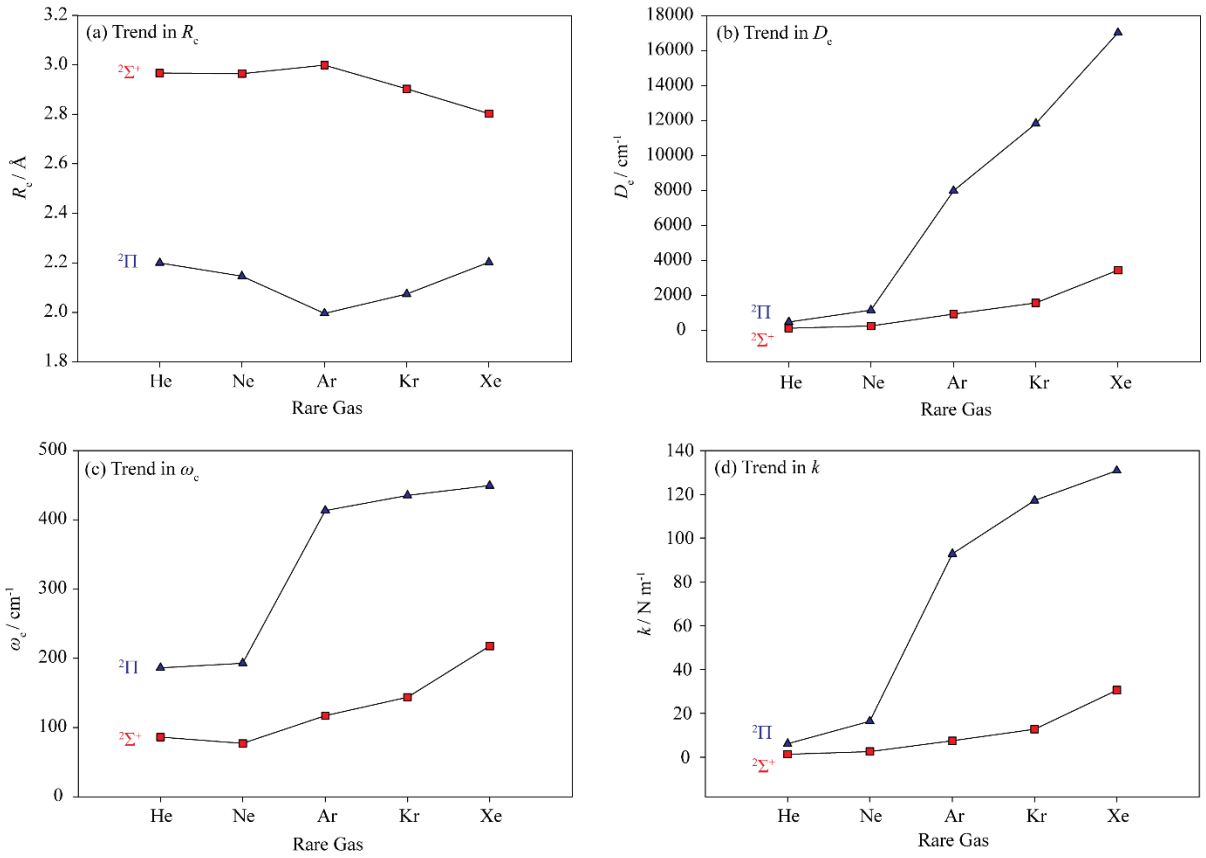
(a) Trend in R_e
R_e / Å
$^2\Sigma^+$
$^2\Pi$
He
Ne
Ar
Kr
Xe
Rare Gas
(b) Trend in D_e
D_e / cm^{-1}
$^2\Pi$
$^2\Sigma^+$
(c) Trend in ω_e
ω_e / cm^{-1}
(d) Trend in k
k / N m^{-1}

Figure 3

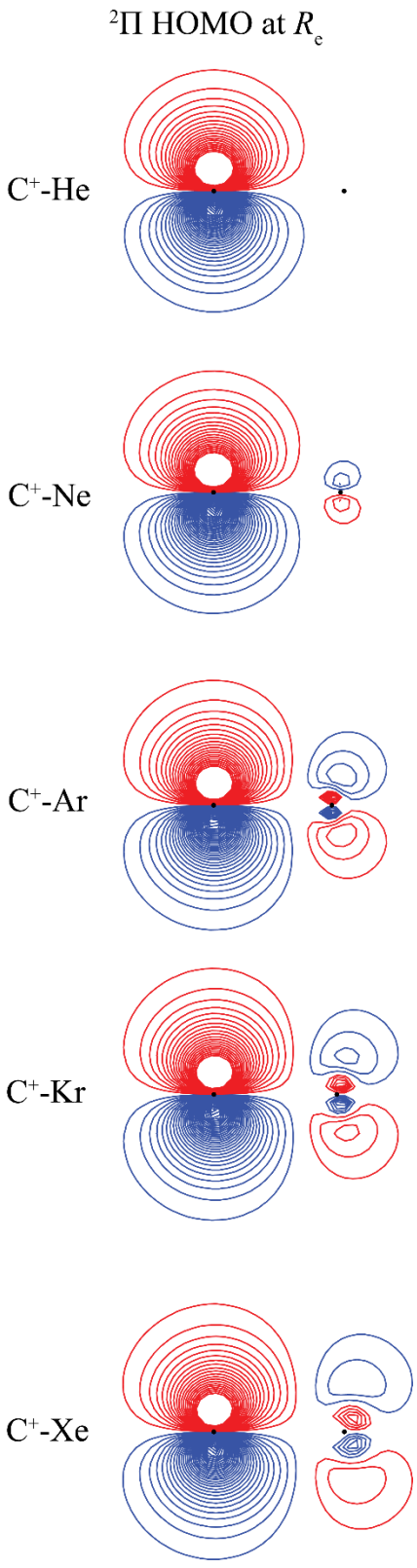

Figure 4

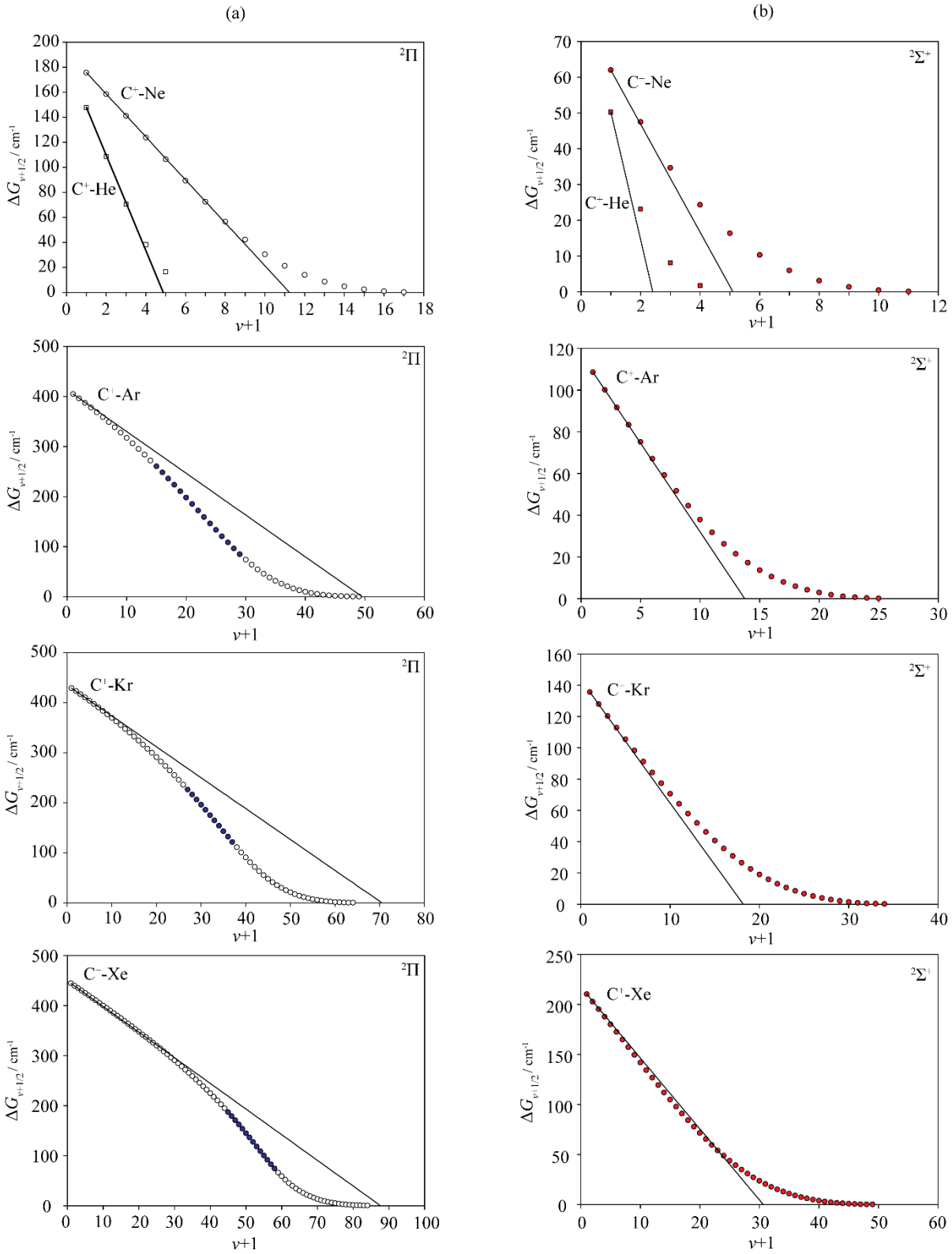
(a)
(b)
$^2\Pi$
$^2\Sigma^+$
C^+-Ne
C^--Ne
C^+-He
C^--He
C^+-Ar
C^--Ar
C^+-Kr
C^--Kr
C^--Xe
C^+-Xe
$\Delta G_{v+1/2}$ / cm^{-1}
v+1

Figure 5

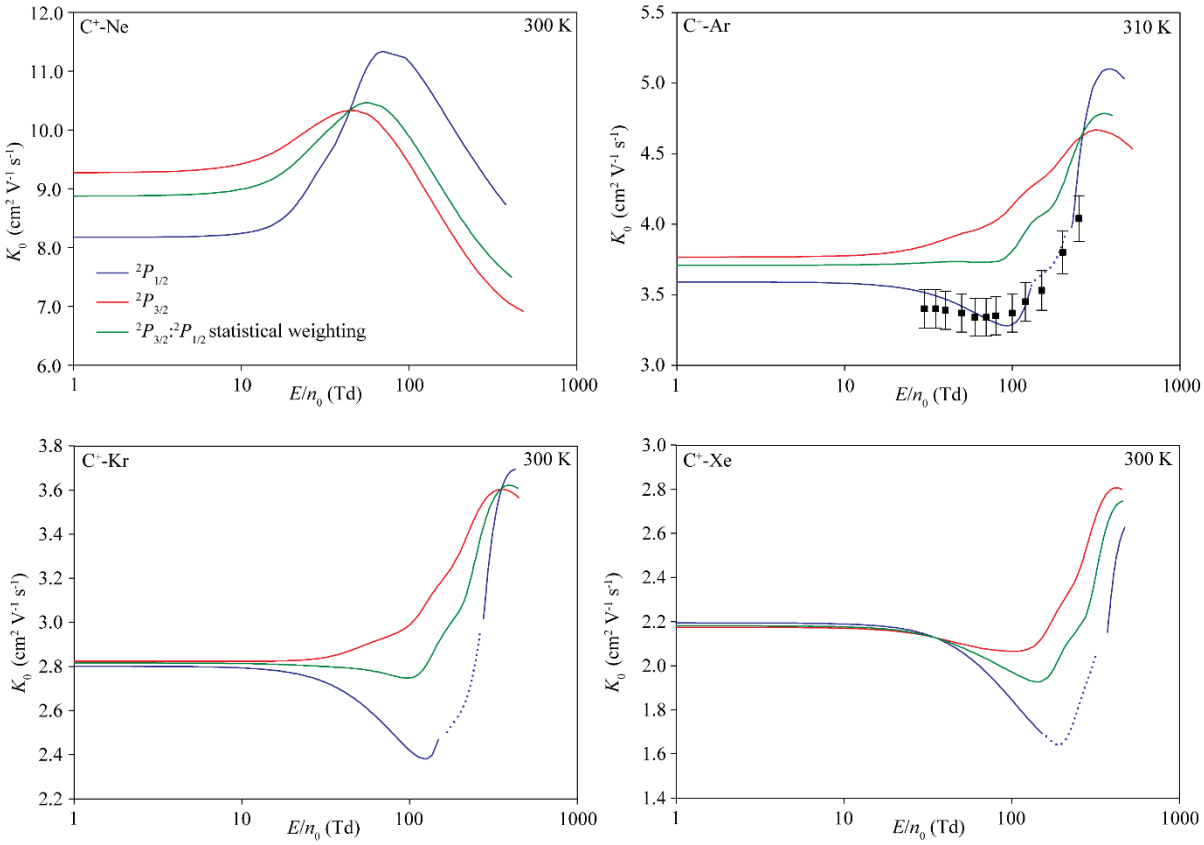
C+-Ne
300 K
C+-Ar
310 K
C+-Kr
300 K
C+-Xe
300 K
K0 (cm2 V-1 s-1)
E/n0 (Td)
2P1/2
2P3/2
2P3/2:2P1/2 statistical weighting

Figure 6

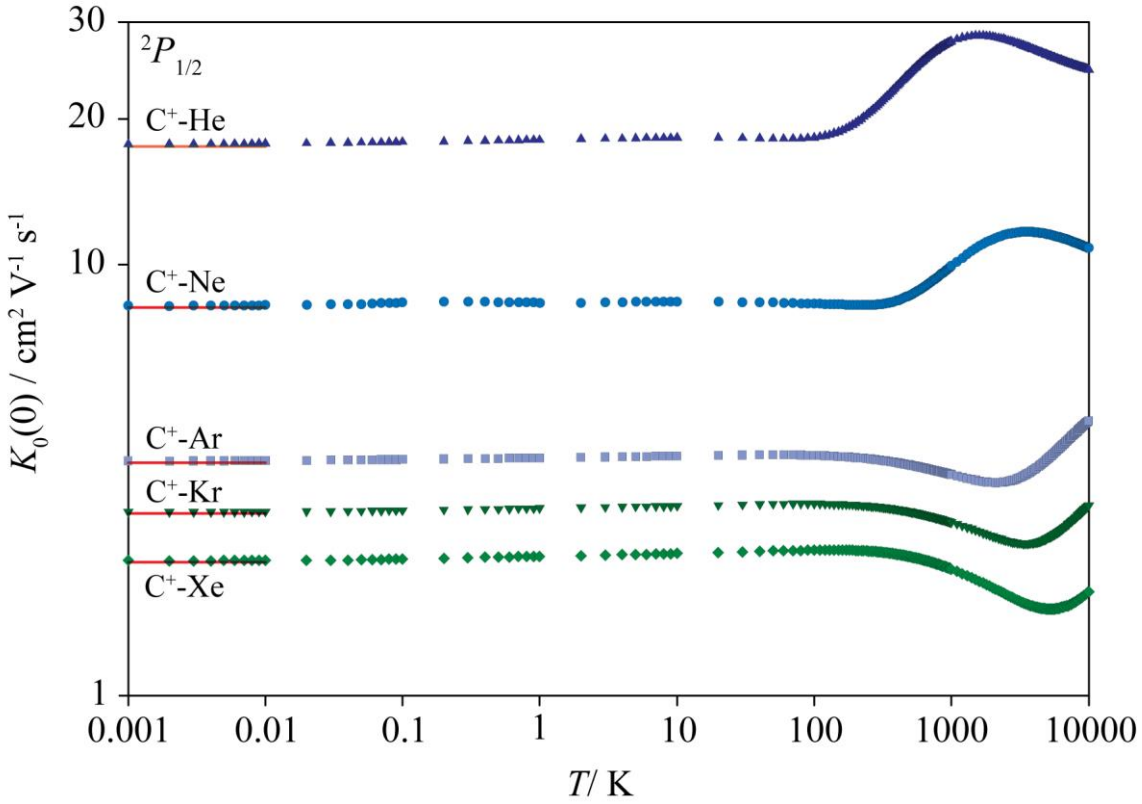
30
20
10
1
$^2P_{1/2}$
C$^+$-He
C$^+$-Ne
C$^+$-Ar
C$^+$-Kr
C$^+$-Xe
$K_0(0)$ / cm^2 V^{-1} s^{-1}
0.001
0.01
0.1
1
10
100
1000
10000
T/ K

References

[1] Petrie S, Bohme DK. 2007 Ions in space *Mass Spec. Rev.* **26**, 258–280. (doi: 10.1002/mas.20114)

[2] Harrison SW Henderson GA, Massa LJ, Solomon P. 1974 Hartree-Fock bound states for molecule-ions HeC^{2+} and HeC^{+} *Astrophys. J.* **189**, 605-607.

[3] Toshima, N. J. 1975 *Phys. Soc. Jpn* **38**, 1464-1470. (doi: 10.1143/JPSJ.38.1464)

[4] Haider SA, Abdu MA, Batista IS, Sobral JH, Luan, X, Kallio, E, Maguire WC, Verigin MI, Singh V. 2009 *D*, *E*, and *F* layers in the daytime at high-latitude terminator ionosphere of Mars: comparison with Earth's ionosphere using COSMIC data J. *Geophys. Res.* **114**, A03311. (doi: 10.1029/2008JA013709)

[5] Fox JL, Paxton LJ. 2005 C and C^{+} in the Venusian thermosphere/ionosphere *J. Geophys. Res.* **110**, A01311. (doi: 10.1029/2004JA010813)

[6] Herbert CG, Johnstone, RAW. 2002 *Mass Spectrometry Basics* Boca Raton, Fl.: CRC Press.

[7] Lade RJ, Claeyssens F, Rosser KN, Ashfold MNR. 1999 193-nm laser ablation of CVD diamond and graphite in vacuum: plume analysis and film properties *Appl. Phys. A* **69**, S935–S939. (doi: 10.1007/s003399900271)

[8] Grutters JPC, Kessels AGH, Pijls-Johannesma M, De Ruysscher D, Joore MA, Lambin P. 2010 Comparison of the effectiveness of radiotherapy with photons, protons and carbon-ions for non-small cell lung cancer: A meta-analysis *Radiotherapy and Oncology* **95**, 32-40. (doi: 10.1016/j.radonc.2009.08.003)

[9] Tuttle, WD, Thorington, RL, Viehland, LA, Wright, TG. 2015 Interaction potentials, spectroscopy and transport properties of $C^{+}(^{2}P_J)$ and $C^{+}(^{4}P_J)$ with helium. *Molec. Phys.* **113**, 3767–3782. (doi:10.1080/00268976.2015.1061153)

[10] Moore CE. *CRC Series in Evaluated Data in Atomic Physics* Boca Raton, Fl.: CRC Press p. 339.

[11] Frenking F, Koch W, Cremer D, Gaus J, Liebman JF. 1989 Neon and argon bonding in first-row cations NeX^{+} and ArX^{+} (X = Li–Ne). *J. Phys. Chem.* **93**, 3410–3418. (doi: 10.1021/j100346a008)

[12] Koch W, Frenking G. Theoretical investigations of small multiply charged cations. II. CNe^{n+} ($1 \leq n \leq 4$). *J. Chem. Phys.* **86**, 5617–5624. (doi: 10.1063/1.452538)

[13] Frenking G, Koch W, Reichel, F, Cremer D. 1990 Light noble gas chemistry: structures, stabilities, and bonding of helium, neon and argon Compounds *J. Am. Chem. Soc.* **112** 4240-4256. (doi: 10.1021/ja00167a020)

[14] Hillier IH, Guest MF, Ding A, Karlau J, Weise J. 1979 The potential energy curves of ArC^{+}. *J. Chem. Phys.* **70**, 864–869. (doi: 10.1063/1.437518)

[15] Wong, MW, Radom, L. 1989 Multiply bonded argon-containing ions: structures and stabilities of XAr^{n+} cations (X = B, C, N; n = 1–3). *J. Phys. Chem.* **93**, 6303–6308. (doi: 10.1021/j100354a009)

[16] McLean AD, Chandler GS. 1980 Contracted Gaussian basis sets for molecular calculations. I. Second row atoms, Z=11–18. *J. Chem. Phys.* **72**, 5639–5648. (doi: 10.1063/1.438980)

[17] Froudakis, GE, Fanourgakis, GS, Farantos, SC, Xantheas, SS. 1998 Binding energies and structures of C^+Ar_n (n = 1–5), clusters from first principles. *Chem. Phys. Lett.* **294**, 109-116. (doi: unknown)

[18] Basurto, E, de Urquijo, J. 2002 Mobility of CF_3^+ in CF_4, CHF_2^+ in CHF_3, and C^+ in Ar. *J. Appl. Phys.* **91**, 36–39. (doi: 10.1063/1.1421034)

[19] MOLPRO is a package of ab initio programs written by H.-J. Werner, P.J. Knowles, G. Knizia, F.R. Manby, M. Schütz, P. Celani, T. Korona, R. Lindh, A. Mitrushenkov, G. Rauhut, K.R. Shamasundar, T.B. Adler, R.D. Amos, A. Bernhardsson, A. Berning, D.L. Cooper, M.J.O. Deegan, A.J. Dobbyn, F. Eckert, E. Goll, C. Hampel, A. Hesselmann, G. Hetzer, T. Hrenar, G. Jansen, C. Köppl, Y. Liu, A.W. Lloyd, R.A. Mata, A.J. May, S.J. McNicholas, W. Meyer, M.E. Mura, A. Nicklaß, D.P. O'Neill, P. Palmieri, D. Peng, K. Pflüger, R. Pitzer, M. Reiher, T. Shiozaki, H. Stoll, A.J. Stone, R. Tarroni, T. Thorsteinsson, M. Wang.

[20] Werner HJ, Knowles PJ, Knizia G, Manby FR, Schütz M. 2012 *WIREs Comput. Mol. Sci.* **2**, 242-253. (doi: 10.1002/wcms.82)

[21] Peterson KA, Dunning, Jr TH. 2002 Accurate correlation consistent basis sets for molecular core–valence correlation effects: the second row atoms Al–Ar, and the first row atoms B–Ne revisited J. *Chem. Phys.* **117**, 10548. (doi: 10.1063/1.1520138)

[22] Peterson KA, Figgen D, Goll E, Stoll H, Dolg M. 2003 Systematically convergent basis sets with relativistic pseudopotentials. II. Small-core pseudopotentials and correlation consistent basis sets for the post-d group 16–18 elements *J. Chem. Phys.* **119**, 11113-11123. (doi: 10.1063/1.1622924)

[23] Halkier, A, Helgaker T, Jørgensen P, Klopper W, Koch H, Olsen J, Wilson AK. 1998 *Chem. Phys. Lett.* **286**, 243-252. (doi: unknown)

[24] Halkier, A, Helgaker T, Jørgensen P, Klopper W, Koch H, Olsen J. 1999 *Chem. Phys. Lett.* **302**, 437-446. (doi: unknown)

[25] Berning A, Schweizer M, Werner HJ, Knowles PJ Palmieri P. 2000 Spin-orbit matrix elements for internally contracted multireference configuration interaction wavefunctions *Mol. Phys.*, **98**, 1823-1833. (doi: 10.1080/00268970009483386)

[26] Lee TJ, Taylor PR. 1989 A diagnostic for determining the quality of single-reference electron correlation methods *Int. J. Quant. Chem*. S23 (1989) 199-207.(doi: 10.1002/qua.560360824)

[27] Gaussian 09, Revision E.01, Frisch MJ, Trucks GW, Schlegel HB, Scuseria GE, Robb MA, Cheeseman JR, Scalmani G, Barone V, Mennucci B, Petersson GA, Nakatsuji H, Caricato M, Li X, Hratchian HP, Izmaylov AF, Bloino J, Zheng G, Sonnenberg JL, Hada M, Ehara M, Toyota K, Fukuda R, Hasegawa J, Ishida M, Nakajima T, Honda Y, Kitao O, Nakai H, Vreven T, Montgomery, Jr. JA, Peralta JE, Ogliaro F, Bearpark M, Heyd JJ, Brothers E, Kudin KN, Staroverov VN, Kobayashi R, Normand J, Raghavachari K, Rendell A, Burant JC, Iyengar SS, Tomasi J, Cossi M, Rega N, Millam JM, Klene M, Knox JE, Cross JB, Bakken V, Adamo C, Jaramillo J, Gomperts R, Stratmann RE, Yazyev O, Austin AJ, Cammi R, Pomelli C, Ochterski JW, Martin RL, Morokuma K, Zakrzewski VG,

Voth GA, Salvador P, Dannenberg JJ, Dapprich S, Daniels AD, Farkas Ö, Foresman JB, Ortiz JV, Cioslowski J, Fox DJ. Gaussian, Inc., Wallingford CT, 2009.

[28] Keith TA, T. K. Gristmill Software, AIMAll, Overland Park, KS, 2011, see aim.tkgristmill.com.

[29] Le Roy RJ. Level 8.0: A Computer Program for Solving the Radial Schrodinger Equation for Bound and Quasibound Levels, University of Waterloo Chemical Physics Research Report CP-663 (2007).

[30] Viehland LA, Chang Y. 2010 *Comput. Phys. Comm.* **181**, 1687-1696. (doi: 10.1016/j.cpc.2010.06.008)

[31] Viehland LA. 1982 *Chem. Phys.* **70**, 149-156. (doi: unknown)

[32] Viehland LA. 1984 *Chem. Phys.* **85**, 291-305. (doi: unknown)

[33] Viehland, LA. 2001 *Comput. Phys. Comm.* **142**, 7-13. (doi: unknown)

[34] Danailov DM, Viehland LA, Johnsen R, Wright TG, Dickinson AS. 2008 *J. Chem. Phys.* **128**, 134302. (doi: 10.1063/1.2898523)

[35] Viehland LA. 2012 *Int. J. Ion Mobil. Spec.* **15**, 21.(doi: 10.1007/s12127-011-0079-4)

[36] www.icecat.laplace.univ-tlse.fr

[37] Plowright, RJ, Gardner, AM, Withers, CD, Wright, TG, Morse, MD, Breckenridge, WH. 2010 Electronic spectroscopy of the 6*p* ← 6*s* transition in Au-Ne: Trends in the Au-RG series. *J. Phys. Chem. A* **114**, 3103–3113. (doi: 10.1021/jp908477q)

[38] Kramida A., Ralchenko Yu., Reader J., and NIST ASD Team (2015). *NIST Atomic Spectra Database* (ver. 5.3), [Online]. Available: http://physics.nist.gov/asd [accessed August 2017]. National Institute of Standards and Technology, Gaithersburg, MD.

[39] Scuseria, GE, Lee, TJ. 1990 Comparison of coupled-cluster methods which include the effects of connected triple excitations. *J. Chem. Phys.* **93**, 5851–5855 (doi:dx.doi.org/10.1063/1.459684).

[40] Breckenridge WH, Jouvet C, Soep B. 1995 Metal atom-rare gas van der Waals complexes in *Advances in Metal and Semiconductor Clusters*, Vol. III, edited by Duncan, M. (JAI, Greenwich), and references therein**. (**eBook ISBN: 9780080545073)

[41] Pilgrim, JS, Yeh, CS, Berry, KR, Duncan, MA. 1994 Photodissociation spectroscopy of M^+-rare gas complexes *J. Chem. Phys.* **100** 7945–7956. (doi: 10.1063/1.466840)

[42] Kaup JG, Leung AWK, Breckenridge WH. 1997 Spectroscopic characterization of the metastable $3p\pi\ ^3\Pi_{0^-,0^+}$ valence states and the $4s^3\Sigma^+$ Rydberg states of the MgK and MgXe van der Waals molecules *J. Chem. Phys.* **107**, 10492–10505. (doi: 10.1063/1.474213), and references therein.

[43] Harris JP, Gardner, AM, Wright, TG, Breckenridge, WH, Viehland, LA. 2012 Interactions in the B^+-RG complexes and comparison with Be^+-G (RG = He-Rn): evidence for chemical bonding. *J. Phys. Chem. A* **116**, 4995-5007. (doi: 10.1021/jp303057x), and references therein.

[44] Cremer D, Kraka E. 1984 Chemical bonds without bonding electron density - does the difference electron-density analysis suffice for a description of the chemical bond? Angew. Chem. Int. Ed. Engl. **23**, 627–628. (doi: 10.1002/anie.198406271)

[45] Viehland LA, Webb R, Lee EPF, Wright TG. 2005 Accurate potential energy curves for HeO^-, NeO^- and ArO^-: spectroscopy and transport coefficients. *J. Chem. Phys.* **122**, 114302. (doi: 10.1063/1.1861874)

[46] Danialov DM, Viehland LA, Johnsen R, Wright, TG, Dickenson, AS. Transport of O^+ through argon gas J. Chem. Phys. **128**, 134302. (doi: 10.1063/1.2898523), and references therein.

[47] Mason EA, McDaniel EW. 1988 *Transport Properties of Ions in Gases* John Wiley and Sons (New York). ISBN: 0-471-88385-9

[48] Yousef A, Shrestha S, Viehland LA, Lee EPF, Gray BR, Ayles VL, Wright TG, Breckenridge WH. 2007 Interaction potentials and transport properties of coinage metal cations in rare gases. *J. Chem. Phys.* **127**, 154309. (doi: 10.1063/1.2774977)

[49] Viehland, LA, Lutfullaeva, A, Dashdorj, J. 2017. Accurate gaseous ion mobility measurements *Int. J. Ion Mobil. Spec.* (In press.) (doi: 10.1007/s12127-017-0220-0)